JOURNAL OF GEOPHYSICAL RESEARCH, VOL. 98, NO. B1, PAGES 557–566, JANUARY 10, 1993

Atmospheric Dust Dispersal Analyzed by Granulometry of the Misers Gold Event

K. H. WOHLETZ AND R. RAYMOND, JR.

Earth and Environmental Sciences Division, Los Alamos National Laboratory, Los Alamos, New Mexico

Granulometric analysis of ejecta from Misers Gold high explosive cratering experiment demonstrates that atmospheric dust dispersal can be evaluated by particle-size distribution data. From size analyses of the Misers Gold preshot test bed alluvium, ejecta, and sweep-up materials collected out to 35 crater radii (1227 m), we find that approximately 5.9×10^6 kg (~11% of the total crater ejecta mass) was depleted from the crater ejecta deposits and likely represents the portion of the cratered mass initially lofted into atmospheric suspension. The dominant size range of this lofted dust was 88 to 2000 μm with a mean diameter by mass of 384 μm. In addition to the dust lofted in the explosion column, dust in the size range of 100–800 μm was swept up from the ground by the explosive air blast and base surge dominantly between ranges of 10 and 18 crater radii (360 and 650 m from ground zero). This sweep-up dust was convectively drawn into the column and contributed up to 2% of the total mass of lofted. Based on the measured abundance of coarse (>250 μm diameter) dust particles in the estimated lofted dust, it is likely that about 70% of this lofted mass fell out within about 1 hour, such that the remaining dust cloud mass was $\sim 1.8 \times 10^6$ kg, which is equivalent to a dust lofted per unit blast yield of 0.5 kT/kT or about 4% of the crater ejecta mass. This study supports the hypothesis that if initial distributions can be constrained, the volume of dust lofted into atmospheric suspension from large surface explosions can be estimated from analysis of particle-size distributions of ejecta deposited near the explosion. This result may have particular applications to study of the atmospheric effects of historic and prehistoric volcanic eruptions.

INTRODUCTION

Atmospheric dust plays a role in global climate variations because of its effect on solar radiation. The 1991 eruption of Mount Pinatubo injected enough volcanic ash into the stratosphere to cause a measurable decrease in global temperature [*McCormick*, 1992]. Atmospheric dust from volcanoes is also recognized as a significant problem for aircraft in that it can cause engine damage [*Casadevall*, 1991]. As well as the volume of dust in atmospheric suspension, its particle-size distribution and composition are other major factors contributing to its global and local effects [*Valero and Pilewskie*, 1992]. In this paper, we investigate a method for calculating the mass of dust lofted by crater-producing explosions that involves size analysis of ejecta deposited near the source.

Our method is based upon some knowledge of the initial size distribution of the ejecta (parent) and its comparison with that of the ejecta deposited on the ground near the explosion (daughter). *Walker* [1980] has applied a similar method to calculating the volume of widely dispersed volcanic ash by comparing the crystal concentration of pumice (parent) to that of sampled ash deposits (daughter). Accordingly, a greater crystal concentration in ash deposits indicates that some of the ash remained in atmospheric suspension and was not emplaced in the sampled deposit. While various methods can be applied to constraining the parental size distribution of ejecta, obtaining accurate daughter distribution data requires assessment of particle size sorting that occurs during ejecta transport to sample locations. We have addressed this problem by using sequential fragmentation/transport analysis [*Wohletz et al.*, 1989], which is described below. In testing our method of dust mass calculation, we have analyzed the dispersal of dust and ejecta from a high explosive cratering test called Misers Gold.

Misers Gold was a surface detonation of 2445 tons of ammonium nitrate-fuel oil blasting agent (ANFO) conducted by the Defense Nuclear Agency for various research purposes (Plate 1). Conducted on alluvial fan sediments at the White Sands Missile Range in New Mexico, the burst excavated a crater with an apparent radius (R) of 35.5 m and a maximum depth of ~17.9 m (K. Benson, personal communication, 1989) and dispersed dust into the atmosphere, much of which fell as ejecta within about 35 crater radii from surface ground zero (SGZ). Some of the lofted dust was swept up from the ground by movement of the explosive airblast and base surge away from the crater; this dust is herein called sweep-up. Along with our particle-size analysis that characterizes the parental alluvial source and daughter samples of the ejecta, a complementary experiment involved WB-57F aircraft sampling of the lofted dust [*Mason et al.*, 1990], and those results have provided a comparative basis for this study.

Ejecta thickness, areal density, and emplacement mode are important aspects of the cratering mechanism [*Post*, 1974; *Piekutowski*, 1977]. Craters from surface bursts have linear crater dimensions proportional to the cube root of yield as primarily determined by the strength of cratered materials. The ejecta, though, are dominantly affected by gravity such that their linear dimensions scale as yield to a power less than a third, and geometric scaling (with normalization to crater radius) is more appropriate [*Lee and Mazzola*, 1989]. In many cases the total volume of crater ejecta does not match that of the crater, and this discrepancy stems from the problems involved with measuring all the crater and ejecta parameters accurately enough to establish a volumetric or mass balance. For example, besides changes in bulk density of cratered materials caused by the blast, a portion of the ejecta is lofted into atmospheric suspension and depos-

Paper number 92JB01888.
0148-0227/93/92JB-01888$05.00

Plate 1. Photograph of the Misers Gold event, a burst of 2445 t of ammonium nitrate and fuel oil (ANFO) on an alluvial fan surface of the White Sands Missile Range, New Mexico, in 1989. Photograph is courtesy of the U.S. Army.

ited downwind far beyond ranges where ejecta thicknesses are measured. However, if one accounts for the volume of atmospherically suspended ejecta, the total ejecta volume exceeds that of the crater. This observation points to the fact that the suspended debris can include materials swept up from the substrate outside of the crater into the convecting cloud by the explosive airblast and/or base-surge induced turbulence. The actual volumetric contribution that swept-up dust makes is also dependent upon factors such as the substrate's size distribution, moisture content, and compaction. The method we describe in this paper circumvents these volumetric measurement problems by addressing the overall size distribution of the cratered materials and how it is modified. The accuracy of this method depends on how accurately one can establish the initial and final particulate size distribution character of crater ejecta.

Forty-eight samples of ejecta/sweep-up debris and 12 samples of the preshot test bed were collected for grain-size analysis (Figure 1). These samples characterize three radial sampling lines: 340° (north), 275° (west), and 225° (south). It is not known if additional sampling on an east radial line would significantly change our results; however, we show that our results from these samples are consistent with those of the aircraft sampling project. The preshot test bed samples are splits taken from 2-m-deep auger holes at distances of 15.9 m, 20.7 m, and 24.4 m from SGZ. The depth of sampling is believed to be a good representation of the total excavated mass, and postshot investigations of several similar tests and Misers Gold, suggest that most of the near to long range ejecta come from the top 2 to 3 m of the test bed (K. Benson, personal communication, 1992). The postshot samples were collected 2 hours after detonation at distances ranging from 118 m (1.4 MPa shock overpressure) to 1227 m (0.01 MPa shock overpressure) from SGZ. The scaled ranges of ejecta and sweep-up samples (3–35R) cover near-field continuous and far-field discontinuous ejecta [*Post*, 1974] but ignore crater lip materials that have a complex origin from the overturned flap [*Roddy*, 1977; *Benson et al.*, 1988]. From observations of the detonation, we suggest that ballistic emplacement and stem fallback controlled ejecta size characteristics out to a range of ~5R, base surge and blast wave sweep-up dominated transport and emplacement of dust over a range of about 5 to 35R, and beyond ~35R most deposition occurred from fallout of suspended dust. Surface winds just prior to shot time were less than several knots, and these may likely have affected dispersal of only the finer suspended dust.

SEQUENTIAL FRAGMENTATION/TRANSPORT ANALYSIS

The analysis follows similar work completed for the Misty Picture test [*Wohletz et al.*, 1988]. Size data are given as mass distributions rather than distributions by particle number, following a newly developed method of particle-size distribution analysis called sequential fragmentation/transport theory (SFT) [*Wohletz et al.*, 1989]. This study constitutes a test of SFT approach for interpreting size-frequency distributions under an experimentally controlled

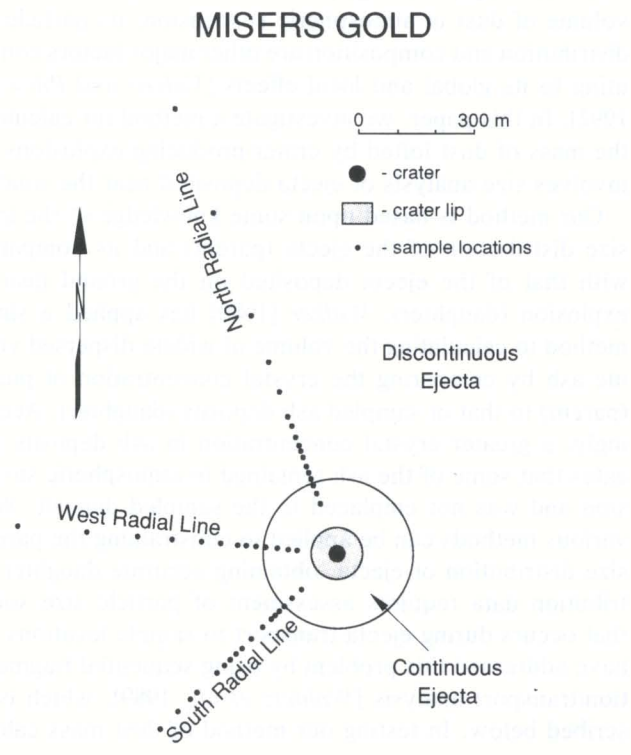

Fig. 1. Plan view of Misers Gold crater and ejecta with locations of ejecta sampling pads along the north (340°), west (275°), and south (225°) radials.

setting. One objective of this application of SFT is to calculate the proportions of parental cratered material and sweep up in the lofted dust cloud and to deduce the modes of the ejecta emplacement.

Unlike previous methods of particle-size distribution analysis that are empirically based (for example, Rosin-Rammler, lognormal, Weibull), SFT is physically based and predicts particle-mass distributions formed by a sequence of fragmentation (comminution) and transport (size sorting) events acting upon an initial mass (m') where the number of particles of a given mass [$n(m)$] is expressed by integral formulations of mass conservation:

$$n(m) = C_1 \int_m^\infty n(m') f(m' \rightarrow m)\, dm', \quad (1)$$

$$n(m, x) = C_2 \int_0^m \int_{x-\xi}^0 n(x', m') p(\xi)\, dx'\, dm'. \quad (2)$$

Equation (1) models fragmentation effects with a transfer function [$f(m' \rightarrow m)$] that expresses the mass dependence of the fragmentation process [*Brown*, 1989]; C_1 and C_2 are constants. Equation (2) includes the transport effects on mass distribution so that the number of particles of a given mass is also a function of transport distance [$n(m, x)$]; the function $p(\xi)$ is the probability that a particle carried from location x' will be deposited at a downstream location x. Where both fragmentation and transport processes are involved in producing the particle-mass distribution of a sample, the solution of equation (2) is preferred, because as *Wohletz et al.* [1989] show, it inherently includes effects of fragmentation:

$$\frac{dM}{d\phi} = K_1 l^6 \exp\left[-\frac{x}{\xi_0}\frac{l^{3(g+1)}}{(g+1)}\right]. \quad (3)$$

This solution gives the mass of particles as a function of logarithmically spaced size bins ($dM/d\phi$), where the logarithmic transformation is $\phi = -\log_2$(diameter in millimeters). K_1 is a normalization parameter set to unity for size-frequency histogram data, l is particle diameter, and x/ξ_0 is a transport range parameter set to unity [*Wohletz et al.*, 1989]. The parameter g in this solution is the exponent in the transport probability function of *Wohletz et al.* [1989]; g is a measure of dispersion and is analogous to the *Brown* [1989] parameter γ, which is the exponent in the transfer function of equation (1). Thus g reflects fragmentation as well as transport mechanisms. For the present work, we refer to g as gamma. *Wohletz et al.* [1989] show that if samples contain particles of distinct shapes and densities, then multiple subpopulations are expected for the size distribution predicted by equation (3).

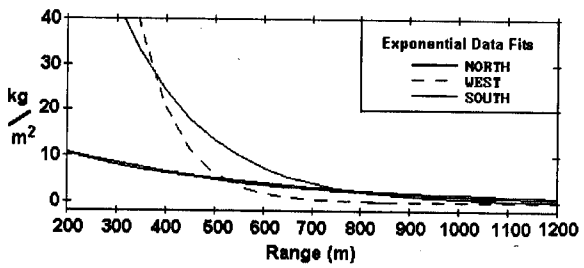

Fig. 2. Ejecta areal density plotted as a function of range from surface ground zero (SGZ). The curves are best fit exponential curves to the data, which were weights of individual samples taken from measured areas on concrete pads at varying ranges.

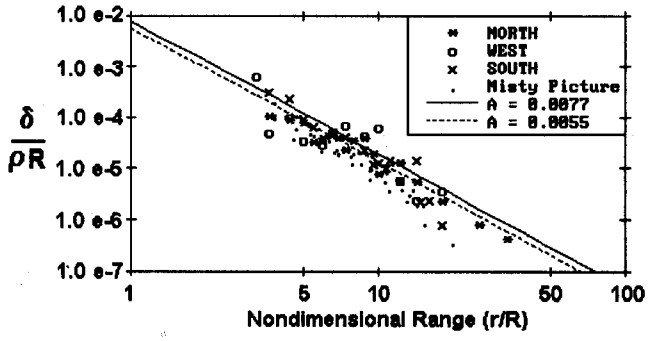

Fig. 3. Scaled ejecta areal density, plotted nondimensionally as $\delta/\rho R$, as a function of nondimensional range, r/R. δ is the measured areal density shown in Figure 3, ρ is the in situ test bed bulk density, R is the apparent crater radius, and r is the sample range from SGZ. The power law fits, shown in the inset, are from *Lee and Mazzola* [1989].

EJECTA AREAL DENSITY

Ejecta samples were collected from the surface of concrete pads emplaced before the shot at varying distances from SGZ along three radial lines. Measurement of the ejecta mass deposited on these pads after the detonation allowed areal densities to be calculated as a function of range (Figure 2). The north line shows considerable variation from the other two, which may be explained by a prevailing wind that carried the lofted cloud (above 800 m altitude) toward the northeast. Figure 3 shows nondimensional areal densities as a function of scaled range. Scaling of these data follows *Lee and Mazzola* [1989], who use nondimensional areal density as a function of nondimensional range:

$$\delta/\rho R = A(r/R)^{-2.6}. \quad (4)$$

In equation (4), δ is areal density (kg/m^2), ρ is the preshot test bed density (taken at 1.7 Mg/m^3), R is the apparent crater radius (35 m), r is the sample range from ground zero, and A approaches a crater-size dependent constant at large r/R. For R = 35 m, *Lee and Mazzola* [1989] found A = 0.0055 for best fits ejecta data from 16 high explosive and nuclear cratering events. The best fit value of the constant A for the Misers Gold data is 0.0077, which is in good agreement considering customary data scatter. For the Misty Picture event of similar design as Misers Gold, measured areal densities [*Wohletz et al.*, 1988] are similar to the present data (Figure 3). It is evident from the data fit (Figure 3) that equation (4) is an appropriate scale function, and *Lee and Mazzola* [1989] discuss the basis for this function.

EJECTA SIZE DISTRIBUTIONS

All samples were dry sieved from 32 mm to 0.045 mm, using sieves of logarithmically decreasing screen sizes (1/2 ϕ (phi) intervals, where $\phi = -\log_2$(diameter in millimeters)). The sieve data were analyzed for individual samples and composite samples. The composite samples represent average test bed and ejecta samples both along each radial

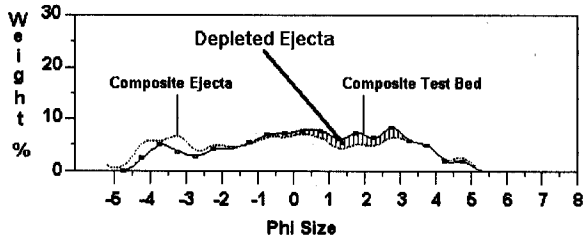

Fig. 4. Size-frequency histogram for composite test bed materials (solid curve with circles at data points) and for composite ejecta/sweep-up samples (dashed curve). The hachured area shows the size range where the composite ejecta are depleted compared to the composite test-bed. The phi (ϕ) size scale is logarithmic ($\phi = -\log_2$(diameter in millimeters) such that $0\phi = 1$ mm, $-4\phi = 16$ mm, and $4\phi = 0.063$ mm.

sampling line as well as for the total; these were constructed by adding weighted averages of corresponding sieve fractions, the weighting factor equal to the areal density times radial distance squared, giving a scaled mass.

In order to compare the ejecta with the test bed materials, the composite test bed distributions were subtracted from the corresponding ejecta composites (Figure 4). The ejecta show depletion in material ranging from about -1ϕ (2.0 mm) to 3.5ϕ (0.088 mm) and a corresponding enrichment of coarser materials in the range of -5 to -1.5ϕ (32.0 to 2.828 mm). The importance of the fines depletion will be discussed later, but for now, we assume that it represents the fraction and size distribution of test bed materials lofted into the atmosphere and not emplaced within the ejecta deposit. For this test bed composite example, the fraction of material lofted is about 11%, and its mean diameter is 384 μm. This estimate is limited by the degree to which the test bed samples represent the size distribution of the total cratered volume, considering that samples were taken only from the upper 2 m of the test bed.

Bulk sample mean diameters and standard deviations for the ejecta are plotted as a function of range in Figure 5. The mean diameters of ejecta show considerable scatter, owing to the nonnormal, polymodal nature of the size-frequency data. Exponential fits of samples from the west and south radial sampling lines show a high of 1.0 to 2.0 mm at ranges from 200 to 300 m (5.7 to 8.6R) with a gradual fining with increasing range. Samples from the north line show a high median diameter near 1.0 mm at a much larger range of 15 to 20R, which likely reflects the affect of the prevailing wind. The standard deviation data are a measure of how size-sorted samples are, and again at ranges from 5 to 9R, the data show highest standard deviations with a gradual decrease at greater range.

The general tendencies in sample size-distribution data shown in Figure 5 can be interpreted further with respect to the transport environment responsible for their origins. Because the observed transport mechanisms of ballistic trajectory, saltation, suspension, and traction (rolling) transport are theoretically sensitive to the mass (hence diameter) of particles being carried, each mechanism should preferentially affect a certain particle size range as a function of the carrier (gas and atmosphere) flux. The following section is an investigation of size-distribution subpopulations that have size ranges that can be interpreted with respect to transport mechanism.

EJECTA SUBPOPULATION ANALYSIS

Inspection of sample size-frequency distributions readily shows that individual samples are polymodal, such that they have variable contribution of several subpopulations. This feature of desert alluvium results from its multistaged evolution from materials transported by wind, water, and mass movement. Sample subpopulation characterization is achieved through SFT by application of a numerical data decomposition and fitting scheme described by *Wohletz et al.* [1989]. This characterization gives the mode (peak location), gamma value (analogous to standard deviation, but with strong physical significance), and fraction of the total sample for each subpopulation. Gamma increases from -1.0 for a population with a flat size-frequency distribution to more positive values for populations that have strong central (peak) tendencies. As populations become better sorted and more evolved, their gamma value increases. *Wohletz et al.* [1989] found that ballistic transport mechanisms typically have g (γ) values (shown in figures as "gamma") less than about -0.60, while traction (rolling) transport shows $-0.65 < g < -0.45$, saltation transport shows $-0.6 < g < 1.0$, and suspended transport shows $-0.40 < g < 0.10$. Figure 6 displays size-frequency histograms for the composite test bed and composite ejecta with their respective size subpopulations identified, as discussed below.

Table 1 summarizes the results of the subpopulation characterization of composite distributions made for the test bed and ejecta samples; these results comprise theoretical distributions that explain better than 95% of the observed sample variance. In Table 1, note the similarities in subpopulation modes for the averaged test bed and ejecta samples, but the gamma values of dispersion show only a crude similarity, while the fractions of subpopulations show that the ejecta has a somewhat higher loading of coarse subpopulations that we will later attribute to winnowing of fine materials into atmospheric suspension. Of the six subpopu-

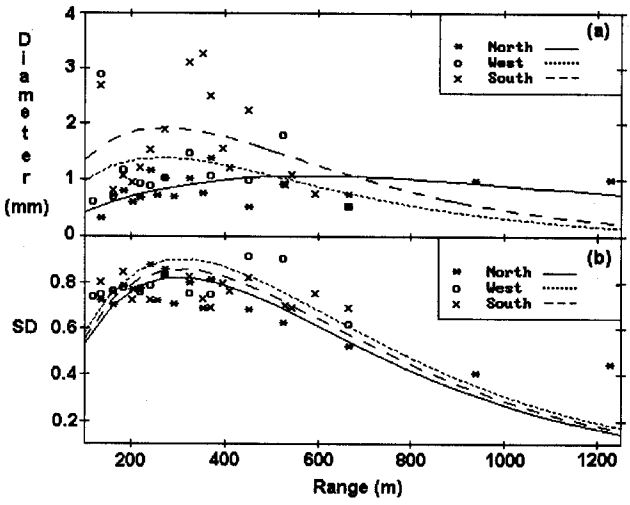

Fig. 5. Plots of (*a*) ejecta/sweep-up mean diameter and (*b*) standard deviation (SD) of diameter as a function of range. Exponential fits are shown for each of the three radials sampled. Scattering of data for mean diameters is attributed to the polymodal, nonnormal population distributions of the ejecta. Maximum values for the curves occur near a range of 300 m (8R), the point at which sweep-up dust begins to contribute significant amounts of fine materials to the base surge.

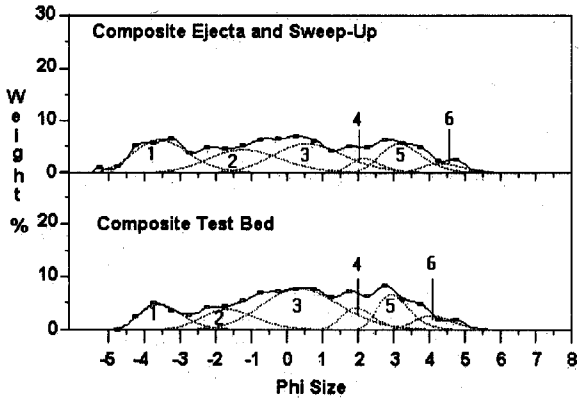

Fig. 6. Size-frequency histograms for the (*a*) composite ejecta/sweep-up materials and (*b*) composite test bed. Spline curves (solid) passing through sieve weight fraction data points (circles) have been fit by addition of six subpopulations (numbered dashed curves). The same subpopulations occur both in the test bed (bulk mean = 0.763 mm, standard deviation = 0.792 log units) composites. See Table 1 for characterization of the subpopulations. Note that the composite test bed distribution shows a marked subpopulation 3 (Table 1 and Figure 7), but this is considered to be an artifact of the averaging, because individual samples of the test bed do not.

lations identified, the first (coarsest) and sixth (finest) are likely affected by data truncation inherent in the sieving technique, which can tend to produce artificially sharp distribution peaks (lower gamma values); interpretation of their character is least certain. For example, the mode of subpopulation 1 is coarser and that of subpopulation 6 is finer than noted in most individual samples. Subpopulation 3 does not show up in all test bed and ejecta/sweep-up samples; on an average it is dominant both in the test bed and ejecta samples.

Mode (peak) diameters for each subpopulation as a function of range are plotted in Figure 7. Note that these modes do not completely correspond to those listed in Table 1. This difference arises because these data are for individual samples, while those of Table 1 are results of analysis of weighted averaged composite distributions, as described above. Not all subpopulations appear in each sample, but inspection of data for ejecta/sweep-up samples (ranges

TABLE 1. Average Subpopulation Characteristics

Subpopulation	Mode ϕ	Mode Millimeters	Dispersion γ	Fraction, wt %
		Test Bed		
1	−3.65	12.553	−0.63	0.13
2	−1.73	3.317	−0.79	0.14
3	0.31	0.807	−0.90	0.42
4	1.90	0.268	−0.40	0.09
5	2.90	0.134	−0.38	0.15
6	4.01	0.062	−0.57	0.07
		Ejecta/Sweep-up		
1	−3.89	14.825	−0.79	0.24
2	−1.53	2.888	−0.88	0.22
3	0.27	0.829	−0.88	0.27
4	1.86	0.275	−0.28	0.06
5	2.86	0.138	−0.64	0.16
6	4.01	0.062	−0.57	0.05

Results of analyses on composite distributions of individual samples weighted by areal density.

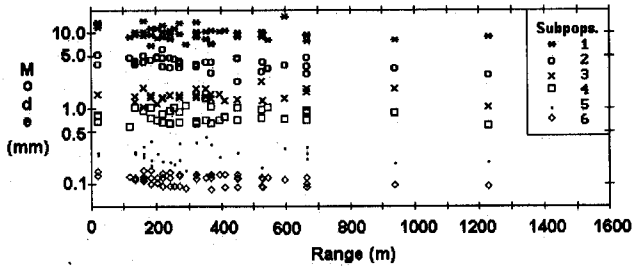

Fig. 7. Plot of composite test bed and ejecta/sweep-up subpopulation modes versus range illustrates the groupings of the identified modes. Samples are plotted at ranges less than 100 m represent test bed samples.

greater than 100 m) shows the test bed subpopulations (range identified in the test bed) are preserved in the ejecta samples. The subpopulations in the ejecta samples, though, are altered, reflecting the effects of postshot ejecta/sweep-up transport mechanisms and possibly variations in test bed materials not recorded by the test bed samples.

Considering the analysis of transport mechanisms of *Wohletz et al.* [1989] and the subpopulation gamma values shown in Table 1, we suggest that, in general, ballistic transport most greatly affects the coarser subpopulations (1 and 2), whereas the fine subpopulation 6 particles are transported in turbulent suspension because they have small associated slip velocities and their initial trajectories are quickly altered by aerodynamic drag and turbulence. Intermediate subpopulations (3, 4, and 5) show dispersion (gamma) values indicative of transport by traction and saltation modifications of their initial ballistic trajectories.

The relative importance of the various transport mechanisms varies with range, which is indicated by a plot of the subpopulation weight fractions *vs* range (Figure 8). Ballistic subpopulations 1 and 2 contribute roughly 10 wt % each showing a slight decrease with range, while the suspended subpopulation 6 decreases with range to about 5 wt %. Subpopulation 3 likely represents particles carried in the

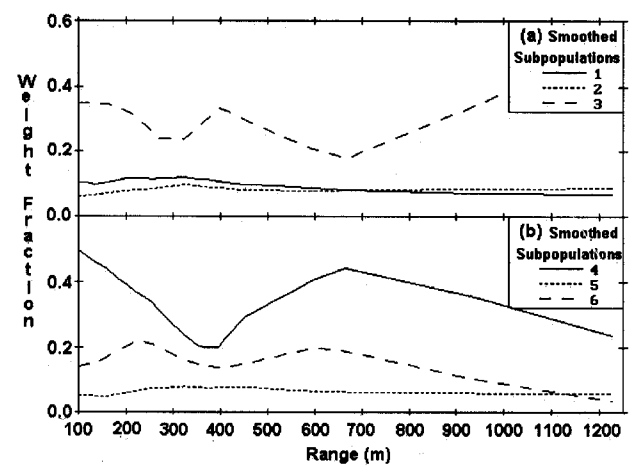

Fig. 8. Plot of composite test bed and ejecta/sweep-up subpopulation fractions versus range. Note the sharp inflections for subpopulations 3, 4, and 5 at ranges of 350 m (10*R*) and 650 m (18*R*), which are interpreted as ranges where sweep-up dominantly occurs. Subpopulation 3 decreases about 15% in response to increases in the abundance of subpopulations 4 and 5, which are believed to reflect additions of sweep-up dust.

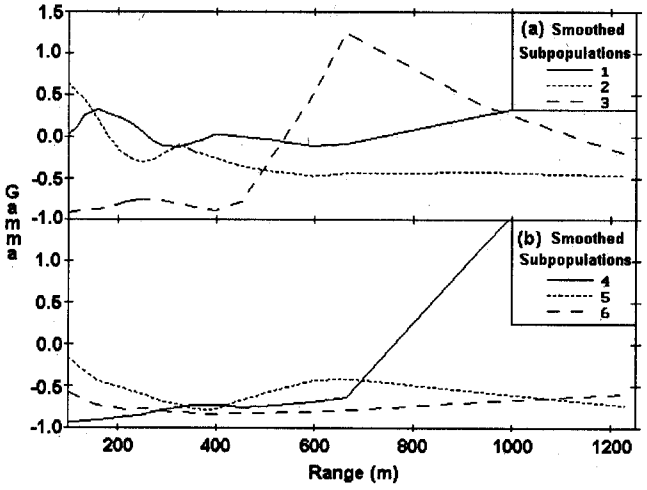

Fig. 9. Plot of composite test bed and ejecta/sweep-up subpopulation dispersions (gamma) versus range. Again sharp inflections occur at ranges of 10 and 18R. Because gamma is indicative of transport mechanism, the inflections suggest that a distinct change in the base surge occurred at these ranges, and as described above, the changes represent the beginning and end of sweep-up by the surge, respectively.

boundary layer by rolling along the substrate. Its fraction shows sharp inflections at about 10R (350 m) and 18R (630 m), beyond which it increase to over 50 wt %, dominating the transport mode. These inflection points are also evident for subpopulations 4 and 6, which represent sizes efficiently carried by saltation. Also, subpopulations 4 and 6 show trends opposite of that of subpopulation 3, which might be indicative of base-surge development. Accordingly, we suggest that at a range of about 10R, the base surge was well developed with sufficient speed to carry particles in saltation, such that traction transport is minimized. By a range of about 18R, the speed of the surge apparently decreased so that particle saltation diminished while their traction movement increased.

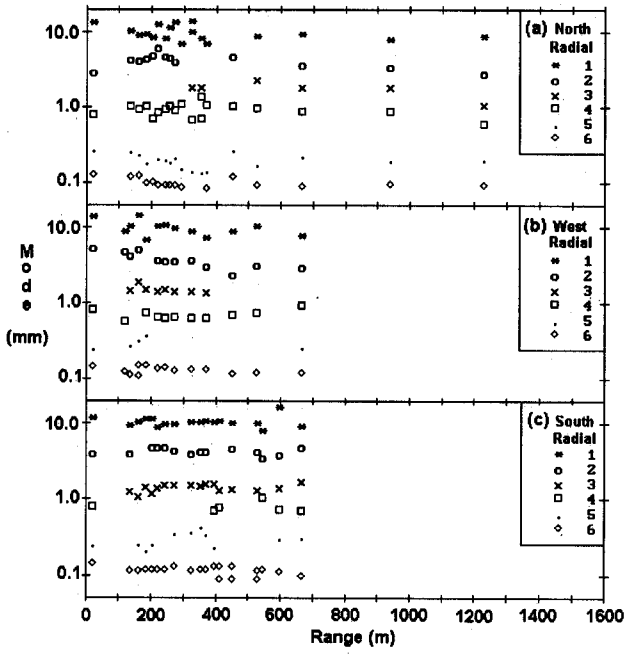

Fig. 10. Plots of subpopulation modes for individual radials. (*a*) The north radial shows great scatter of subpopulation modes, which is indicative of the affect of prevailing wind on the ejecta/sweep-up dispersal. (*b*) The west radial and (*c*) the south radial show tight groupings of subpopulation modes. These data show the appearance and disappearance of individual subpopulations with increasing range.

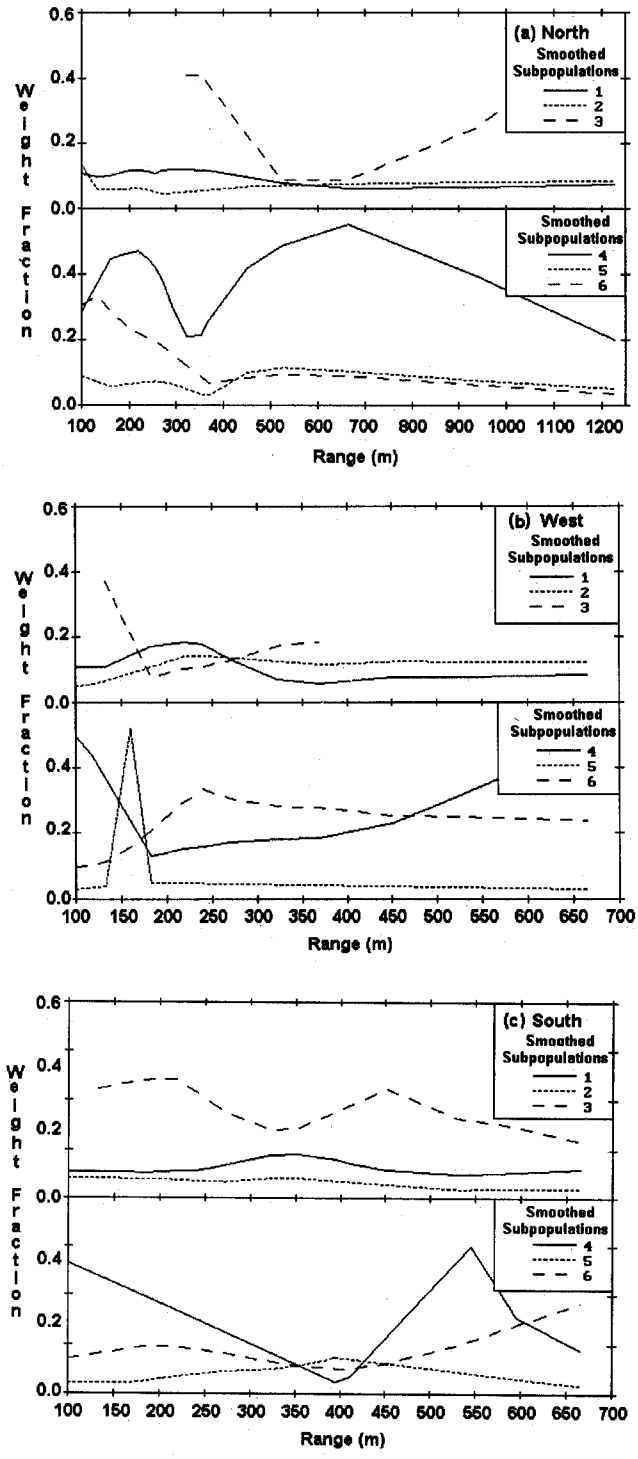

Fig. 11. Plots of subpopulation fractions for the (*a*) north, (*b*) west, and (*c*) south radials, showing the variation in range where sharp inflections in subpopulation abundance occur, especially in subpopulations 3, 4, and 5, which is likely a function of base surge/sweep-up.

Apparently, transport mechanisms evolved down range in response to sorting caused by separation of finer debris from

the coarse. This observation is supported by plots of SFT γ values with range (Figure 9). Ballistic subpopulation 2 shows γ decreasing down range to a well developed value near -0.5; subpopulation 1 has a γ value that increases down range, perhaps reflecting the artificial effect of coarse data truncation by sieve measurements. Subpopulation 6 (suspension) shows little variation with range, probably because it decoupled from the base surge cloud early in its evolution. The traction subpopulation (3) shows gamma evolving quickly from ranges of about $10R$ to a maximum at about $18R$, after which as the subpopulation fraction increases (Figure 8), it looses some of its definition in gamma. Saltating subpopulations 4 and 5 show best development beyond a range of $18R$.

In further documentation of the down-range evolution of subpopulations, Figures 10–12 show the variations in subpopulation mode, fraction, and γ for each of the three sampled radial lines. Of the three radial sampling lines, the north one shows the most scatter in subpopulation modes (Figure 10*a*), which is evidence that prevailing wind affected the emplacement of the ejecta. Subpopulation fractions (Figure 11) and gamma values (Figure 12) show one or more distinct inflection points (as discussed above), which points to major changes in the boundary layer of the base surge. For the north radial, these inflections show up at a range of $10R$ and $18R$. The west radial shows only one major inflection point at about 5 to $7R$ (~250 m). The south radial like that of the north shows an inflection point at $10R$ and an indistinct one, possibly developing at the limit of our sampling near $18R$.

The interpretation of these inflection points is that they represent points at which the base surge became well developed ($10R$ along the north and south radials) and then started waning and detaching from the substrate ($18R$ along the north radial). At ranges closer than 5 to $10R$, the deposition of ejecta was highly disorganized; here fallback ejecta from the stem collapse impinged the ground and began lateral movement as an evolving base surge. At greater ranges (between about $10R$ and $18R$), dust swept up into atmospheric suspension by the base surge was likely greatest, as shown by the decrease in subpopulations 4 and 5 weight fractions (Figures 9 and 11) over this range.

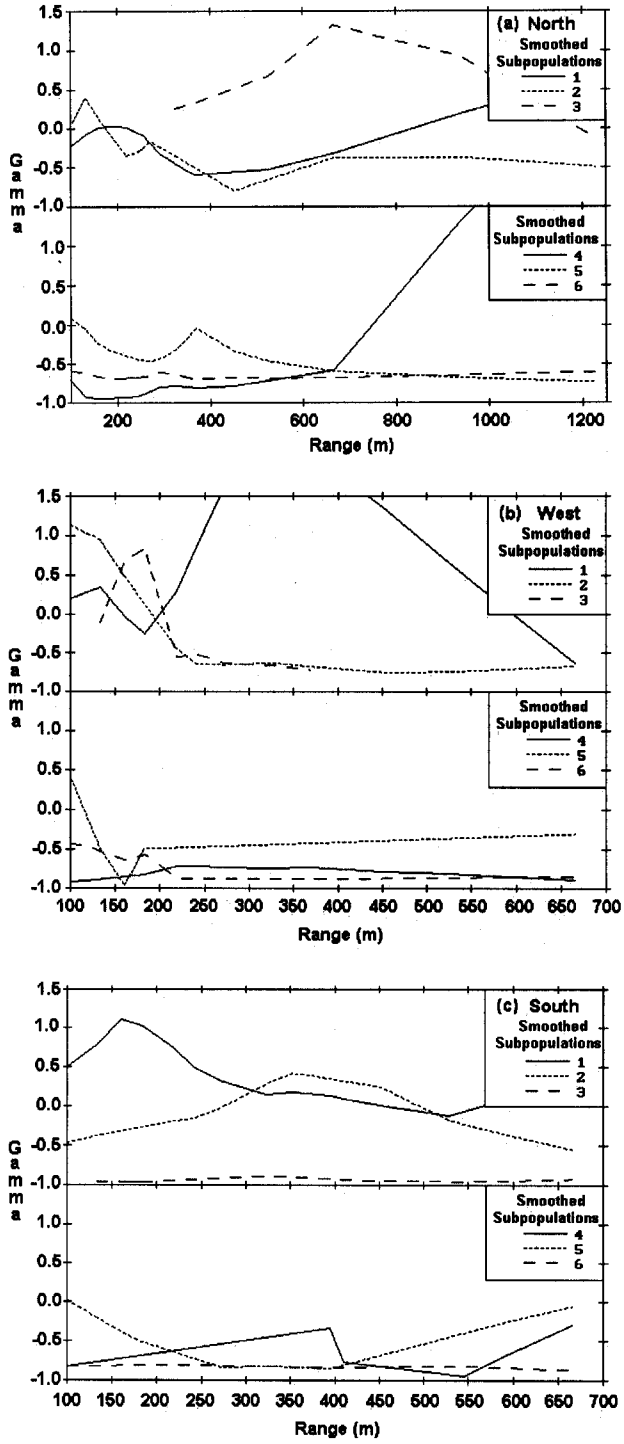

Fig. 12. Plots of subpopulation gamma values for the (*a*) north, (*b*) west, and (*c*) south radials. For the north radial, subpopulations 3 and 4 show high gamma values, indicative of well-developed transport mechanism, which are thought to be traction and saltation transport for these subpopulations, respectively. The development of these transport mechanisms reflect the sweep-up process occurring in the base surge between ranges of 10 and $18R$. Base surge sweep-up is less apparent in the west and south radials, but the west radial shows complicated variations at ranges less than 200 m ($6R$), which may reflect the affects of ballistic ejecta and stem fallback.

Discussion of the Ejecta Size Analysis

Perhaps the most important finding of the size analysis is estimation of the depleted mass in the ejecta found by subtracting composite ejecta/sweep-up samples from composite test bed samples. By assuming that the cratering and ejecta depositional processes caused very little changes in individual particle sizes, we conclude that this depleted mass represents the portion of the ejecta lofted into atmospheric suspension and not deposited in the ejecta deposit. We believe that this assumption is valid because the test bed subpopulations remain fairly constant in character when comparing preshot and postshot samples (Table 1). Furthermore, the size distribution of this calculated lofted dust generally falls within the 44 to 1000 μm size range, the lower portion of which roughly corresponds to those sizes captured by the aircraft filters. Another interpretation of the apparent depleted mass is that moisture present in the ejecta caused aggregation of particles in fine subpopulations to form coarse particles. This possibility is indicated in Figure 8 where subpopulation 3 increases in fraction down range while subpopulations 4 and 6 decrease. However, we did not observe a significant portion of aggregated particles in our samples, and the complex downrange evolution of particle

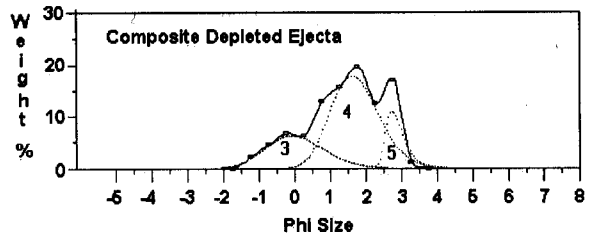

Fig. 13. Size-frequency histogram for the depleted mass of the composite ejecta, illustrated in Figure 2. Subpopulations 3, 4, and 5 are represented by this distribution (curve with circles). This distribution constitutes 11.3% of the ejecta, and it represents the material lofted and not precipitated in the ejecta deposit. It has a mean diameter of 384 μm, and subpopulation 4 dominates the distribution. See Table 2 for characteristics of the depleted subpopulations.

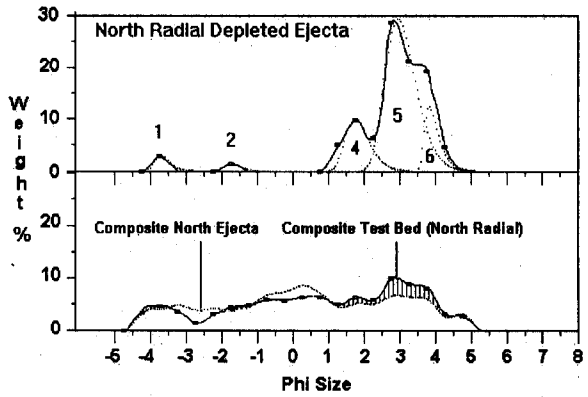

Fig. 14. Size-frequency histograms for the north radial. The bottom plot shows the composite test-bed (solid curve with circles at data points) and the composite ejecta (dashed curve). The hachured area illustrates the fraction of depleted material in the ejecta, which has presumably been lofted, such that it did not precipitate within the sampled ejecta range. The top plot shows the distribution of the depleted material with subpopulation 5 dominating. Subpopulations 1 and 2 probably represent the portions (17 and 10% of those test bed subpopulations, respectively) of coarse material blown by the prevailing wind out of the sample area. See Table 2 for characteristics of the depleted subpopulations.

transport mechanism, as described above, is also a likely explanation of subpopulation fraction changes.

The size-frequency histogram of the depleted mass is shown in Figure 13 to have contributions from subpopulations 3, 4, and 5 (Table 2), which forms the basis for a model of the size distribution of lofted dust. In comparison of the ejecta with the test bed materials shown in Table 2, subpopulation 4 (337 μm) has been greatly enriched (4.43 times) at the expense of subpopulation 3 (0.41 times) and subpopulation 5 (0.65 times). A comparison of composite ejecta along each of the three radial lines with their respective composite test bed materials is depicted in Figures 14–16. The north radial line shows 11.7 wt % depletion of dust sizes mostly between 45 and 354 μm (160 μm mean), the west and south radial lines show depletions of 12.8 and 23.3 wt %, respectively, of coarser dust sizes between 125 and 2000 μm (574 and 493 μm mean diameters, respectively). The overall, coarser-grained, depleted masses west and south of the crater can be attributed to the effects of the prevailing wind. For the north radial, depleted mass subpopulations 1 and 2 do appear in small amounts, suggesting that the prevailing wind carried some of these large sizes beyond the sampled range. These results are supported by observations of the atmospheric dust cloud precipitating pellet-sized dust grains well beyond the sampled range of the north radial. This same precipitation of pellet-sized ejecta apparently did not occur beyond the sampling range of the west and south radials.

These estimations of lofted dust are supported by the results from the aircraft filter analysis [*Mason et al.*, 1990]. The comparison is somewhat complicated by the timing of the aircraft sampling and the fact that the aircraft filter samplers have air flow characteristics that allow capture of particles less than ~250 μm in diameter. The estimates provided by indium tracers emplaced in the test bed and subsequently analyzed in aircraft filter samples indicate the

TABLE 2. Size Characteristics of the Estimated Lofted Mass

Fraction,* wt %	Mean, μm	Subpopulation	Mode, mm	Dispersion γ	Fraction	Enrichment Factor†
			North Radial			
11.70	160	1	13.642	2.0	0.03	0.17
		2	3.864	1.0	0.02	0.10
		4	0.344	−0.1	0.18	2.00
		5	0.132	−0.34	0.63	1.58
		6	0.072	2.61	0.13	1.08
			West Radial			
12.79	574	3	0.946	−0.86	0.71	0.81
		4	0.291	−0.64	0.25	25.00
		5	0.179	1.50	0.08	0.80
			South Radial			
23.29	493	3	0.678	−0.88	0.76	0.91
		4	0.308	−0.19	0.22	3.67
		5	0.171	1.63	0.06	0.60
			Composite Radial			
11.29	384	3	1.087	−0.82	0.26	0.41
		4	0.337	−0.74	0.62	4.43
		5	0.154	1.00	0.15	0.65

*Amount of mass apparently depleted from the ejecta distribution relative to the test bed.
†Ratio of the depleted subpopulation fraction to the corresponding amount in the test bed.

apparent total lofted mass at 1.79×10^6 kg (dust lofted per unit blast yield = 0.45 kT/kT) [*Mason et al.*, 1990].

If the mass of dust lofted into atmospheric suspension is proportional to apparent crater volume (V_a), then we can estimate the lofted mass from the size distribution data. The apparent crater volume of Misers Gold can be approximated as

$$V_a = (R/b)^3, \quad (5)$$

from scaling of crater volume in alluvium [*Vortman*, 1968], where $b = 1.13$ for Misers Gold. Based upon the depleted mass calculations described above and assuming an average bulk density of cratered alluvium as 1.7×10^3 kg/m^3, we estimate that 5.9×10^6 kg (1.5 kT/kT) of dust was lofted (11.3% of the crater ejecta mass). Although this result is 3.3 times larger than that estimated from aircraft filter samples, it is in surprising agreement when considering the particle size ranges and sampling times involved. Noting the coarse size cutoff of the aircraft samples at ~250 μm, we find that our calculated depleted mass (Figure 13) shows 69 wt % of the size distribution to be coarser than 250 μm in diameter. Excluding this coarser fraction, our estimation of lofted mass becomes 1.8×10^6 kg (0.46 kT/kT or 3.5% of the crater ejecta mass) and closely agrees with the findings of *Mason et al.* [1990]. We consider this latter estimate to be a better representation of the dust mass lofted, because it represents the fraction of dust with substantial atmospheric resident time. The aircraft samples were obtained at progressively higher altitudes between 0.875 and 4.990 km (cloud top) from 16 to 52 min after detonation, respectively, with greatest cloud density measured at an altitude of about 3.6 km at 39 min [*Mason et al.*, 1990]. For the range of observed dust particle sizes >250 μm in diameter, *Brissette and Lajoie* [1990] have determined terminal fall speeds in turbulent suspensions of finer dust to be from 1 to 10 m/s. Applying these fallout rates to the coarser ejecta indicates that the lofted cloud will be depleted in particles >250 μm diameter in a little over 1 hour, even for fallout from the cloud top.

There are size data inflection points at distances of 10 and 18R (Figures 8–12). The best interpretation of these inflections are based upon inferences in mechanism of ejecta emplacement. The boundary layer within the base surge was likely best developed while the surge evolved from carrying ejecta and sweep-up dust in a dominantly saltating mode to a dominantly traction mode (R = 10 to 18; Figures 8 and 9). Over this range, the addition of sweep-up dust by the base surge was probably greatest, because the boundary layer sheer stress was likely at its highest. For example, subpopulation 3 increases in relative fraction by nearly 15 wt % over this range in response to corresponding decreases in finer subpopulations 4 and 6 (Figure 8). If the decreases in subpopulations 4 and 6 reflect the dust swept up into the lofted cloud, then base-surge sweep-up dust possibly contributed 1–2 wt % (15% × 11.3%) to the total for the lofted cloud.

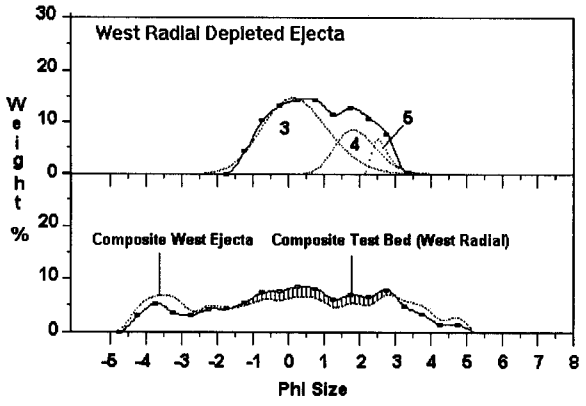

Fig. 15. Size-frequency histograms for the west radial. The bottom plot shows the composite test bed (solid curve with circles at data points) and the composite ejecta (dashed curve). The hachured area illustrates the fraction of depleted material in the ejecta, which has presumably been lofted, such that it did not precipitate within the sampled ejecta range. The top plot shows the distribution of the depleted material with subpopulation 3 dominating. See Table 2 for characteristics of the depleted subpopulations.

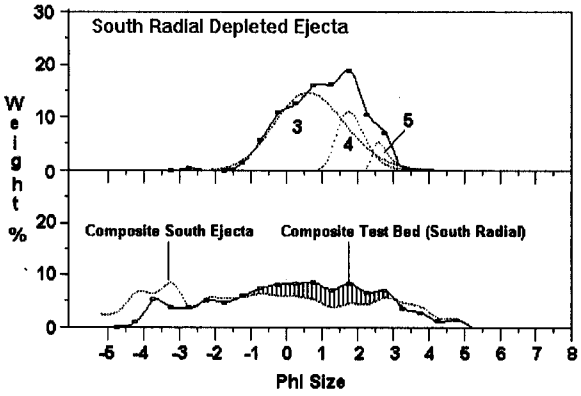

Fig. 16. Size-frequency histograms for the south radial. The bottom plot shows the composite test bed (solid curve with circles at data points) and the composite ejecta (dashed curve). The hachured area illustrates the fraction of depleted material in the ejecta, which has presumably been lofted, such that it did not precipitate within the sampled ejecta range. The top plot shows the distribution of the depleted material with subpopulation 3 dominating. See Table 2 for characteristics of the depleted subpopulations.

Dust lofted by cratering events both man-made and natural (volcanic) poses an important threat to both commercial and military aviation. Large particles may cause significant abrasion on aircraft surfaces and at supersonic speeds may penetrate the aircraft surfaces. Fine particles in dilute atmospheric suspension may be difficult or impossible for pilots or navigation systems to detect. In the case of this study, we did not carry out size characterization of particles finer than 0.045 mm. However, this fine fraction generally contributed <5% of the initial test bed material. Because these fine particles sustain tiny slip velocities and constitute a minor mass fraction, we believe they pose a relatively small damage potential to aircraft compared with that of the coarser fractions. Still, the fine dust particles are potentially more damaging when ingested by jet engines, because they can readily infiltrate lubrication systems, and they contain a higher concentration of low melting temperature minerals (for example, silicate glass and clays) that can adhere to engine surfaces [*Casadevall*, 1991].

The granulometry technique we have described in this paper demonstrates the potential for predicting the amounts and size distributions of dust clouds emplaced in the atmosphere by man-made and volcanic explosions. The method depends on obtaining representative size distribution characterizations of both the parent (crater substrate or initial

magmatic) and the daughter ejecta deposited on the ground near the explosion site. With careful ground sampling and dust size analysis, this technique can provide information important for aviation and global climate predictions at relatively small expense compared to atmospheric sampling missions or sophisticated Lidar experiments.

Acknowledgments. This work was done under the auspices of the U.S. Department of Energy with funding provided by the Defense Nuclear Agency under IACRO 89-830 task code RA/RY. We thank Major D. Wade of the U.S.A.F. for guidance in this work. We also thank Allen Mason and Greg Bayhurst for providing logistical support in sampling for this experiment and Ken Benson for kindly offering data from his study of the cratering phenomena. Tom Mazzola and Ken Benson gave thoughtful reviews.

REFERENCES

Benson, K. A., D. Chavez, P. Roupas, R. Henry, and D. J. Roddy, Cratering and related effects for the Misty Picture event, *Rep. NMERI WA6-17 (6.03)*, N. M. Eng. Res. Inst., Albuquerque, March 1988.

Brissette, F. P., and J. Lajoie, Depositional mechanics of turbulent nuées ardentes (surges) from their grain sizes, *Bull. Volcanol.*, *54*, 60–66, 1990.

Brown, W. K., A theory of sequential fragmentation and its astronomical applications, *J. Astrophys. Astron.*, *10*, 89–112, 1989.

Casadevall, T. J. (Ed.), First International Symposium on Volcanic Ash and Aviation Safety, Program and Abstracts, *Circ. 1065*, 58 pp., U.S. Geol. Surv., Reston, Va., 1991.

Lee, C. K. B., and T. A. Mazzola, Ejecta scaling laws for craters in dry alluvial sites, *J. Geophys. Res.*, *94*, 17,595–17,605, 1989.

Mason, A. S., D. L. Finnegan, G. K. Bayhurst, R. Raymond Jr., R. C. Hagan, G. Luedemann, and K. H. Wohletz, Dust collection and cloud characterization, *Rep. LA-CP-90-26*, pp. 1–38, Los Alamos Natl. Lab., Los Alamos, N. M., 1990.

McCormick, M. P., Initial assessment of the stratospheric and climatic impact of the 1991 Mount-Pinatubo eruptions—Prologue, *Geophys. Res. Lett.*, *19*, 149–150, 1992.

Piekutowski, A. J., Cratering mechanisms observed in laboratory-scale high-explosive experiments, in *Impact and Explosion Cratering*, edited by D. J. Roddy, R. O. Peppin, and R. B. Merrill, pp. 67–102, Pergamon, New York, 1977.

Post, R. L., Ejecta distributions from near-surface HE burst, *Rep. AFWL-TR-74-51*, Air Force Weapons Lab., Kirtland Air Force Base, N. M., 1974.

Roddy, D. J., Large-scale impact and explosion craters: Comparisons of morphological and structural analogs, in *Impact and Explosion Cratering*, edited by D. J. Roddy, R. O. Peppin, and R. B. Merrill, pp. 185–246, Pergamon, New York, 1977.

Valero, F. P. J., and Pilewskie, P., Latitudinal survey of spectral optical depths of the Pinatubo volcanic cloud—Derived particle sizes, columnar mass loadings, and effects on planetary albedo, *Geophys. Res. Lett.*, *19*, 163–166, 1992.

Vortman, L. J., Craters from surface explosions and scaling laws, *J. Geophys. Res.*, *73*, 4621–4636, 1968.

Walker, G. P. L., The Taupo Pumice: product of the most powerful known (ultraplinian) eruption? *J. Volcanol. Geotherm. Res.*, *8*, 69–94, 1980.

Wohletz, K. H., R. Raymond Jr., G. Rawson, and T. Mazzola, Analyses of sweep-up, ejecta, and fallback material from the 4250 metric ton high explosive test "Misty Picture," in *Smoke/Obscurants Symposium XII*, pp. 1–18, The Johns Hopkins University, Baltimore, Md., 1988.

Wohletz, K. H., M. F. Sheridan, and W. K. Brown, Particle size distributions and the sequential fragmentation/transport theory applied to volcanic ash, *J. Geophys. Res.*, *94*, 15,703–15,721, 1989.

R. Raymond, Jr., and K. H. Wohletz, Los Alamos National Laboratory, EES-1, Geology/Geochemistry, MS D-462, Los Alamos, NM 87545.

(Received August 21, 1991;
revised July 13, 1992;
accepted August 12, 1992.)